Revisiting wind wave growth with fully coupled direct numerical simulations

Jiarong Wu, Stéphane Popinet, Luc Deike

Revisiting wind wave growth with fully-coupled direct numerical simulations

Jiarong Wu[1], Stéphane Popinet[2], and Luc Deike[1,3,†]

[1]Department of Mechanical and Aerospace Engineering, Princeton University, Princeton, NJ 08544, USA

[2]Institut Jean Le Rond d'Alembert, CNRS UMR 7190, Sorbonne Université, Paris 75005, France

[3]High Meadows Environmental Institute, Princeton University, Princeton, NJ 08544, USA

(Received xx; revised xx; accepted xx)

We investigate wind wave growth by direct numerical simulations solving for the two phase Navier-Stokes equations. We consider ratio of the wave speed c to wind friction velocity u_* from $c/u_* = 2$ to 8, i.e. in the slow to intermediate wave regime; and wave steepness ak from 0.1 to 0.25; the two being varied independently. The turbulent wind and the travelling, nearly monochromatic waves are fully coupled without any subgrid scale models, with a turbulent boundary layer friction Reynolds number of 720. We observe wave growth from wind energy input, in quantitative agreement with that computed from the extracted surface pressure distribution, which confirms the leading role of the wind pressure forcing. The phase shift and the amplitude of the surface pressure distribution are systematically reported. We find that the wave drag force is not a strong function of c/u_* but closely related to ak. The wave growth rate we obtain agree with previous experimental and numerical studies. We make an effort to clarify various common underlying assumptions, and to reconcile the scattering of the data between different experimental results and the theories, as we revisit this longstanding problem with new numerical evidence.

Key words:

1. Introduction

1.1. *Motivation*

Wind waves, i.e. waves forced by local wind, play an active role in many air-sea interaction processes (Sullivan & McWilliams 2010; Cavaleri *et al.* 2012; Deike 2022). The growth of waves under wind forcing, however, is still an area with open questions, in terms of the exact mechanism responsible for wave growth. A number of theories (Jeffreys 1925; Miles 1957; Belcher & Hunt 1993) of varying complexity have been proposed over the years (see Janssen (2004) for a review) but their applicability is unclear due to lack of direct empirical evidence. Field campaigns (Snyder *et al.* 1981; Donelan *et al.* 2006) and laboratory scale experiments (Peirson & Garcia 2008; Grare *et al.* 2013; Shemer 2019; Buckley *et al.* 2020) have reported growth rates that can scatter by an order of magnitude, and sometimes largely deviate from the theoretical predictions (see Peirson &

† Email address for correspondence: ldeike@princeton.edu

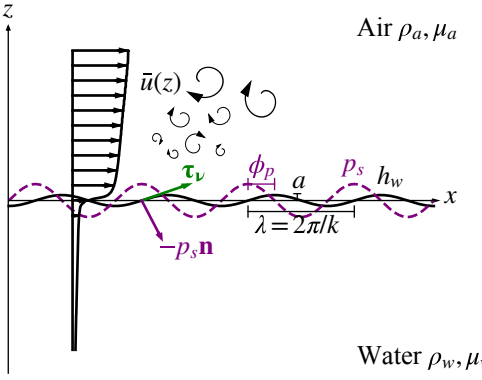

FIGURE 1. A sketch of the wind-wave problem. The surface stress consists of the normal pressure stress ($p_s\boldsymbol{n}$), and the viscous stress $\boldsymbol{\tau}_\nu$. The correlation of the surface pressure p_s (purple dotted line) with the surface elevation slope $\partial h_w/\partial x$ is generally thought to be the major contribution to the wave growth (see (1.1)). In this paper we consider wind blowing in x direction, and therefore no misalignment effect is discussed. The wind blows from left to right, and the maximum of the pressure distribution is on the windward face for slow moving waves. The phase shift ϕ_p denotes the phase lag of the pressure maximum to the wave crest.

Garcia 2008). Since the wind forcing forms the basic source term for any operational wave model (Janssen 2004), it is important to continue to improve our physical understanding of the dynamic processes controlling the wave growth rate in different wind-wave regimes.

1.2. *Problem formulation*

The dynamics of the wind wave interaction is a coupled two-phase flow, as sketched in figure 1. The wind (of density ρ_a) blows across a moving wavy water surface $h_w(x, y, t)$ (of density ρ_w), and the structure of the atmospheric turbulent boundary layer is altered. The resulting wave coherent surface wind stress in turn transfers energy into the waves. The wind stress at the surface consists of two parts, the viscous stress ($\boldsymbol{\tau}_\nu$) mostly in the tangential direction, and the pressure stress ($p_s\boldsymbol{n}$) in the normal direction, see figure 1. It has been generally agreed on that for gravity waves, the wave growth mostly results from the work done by the surface air pressure, although the wave coherent viscous stress can play a part at low steepness and gravity-capillary waves (Peirson & Garcia 2008; Buckley *et al.* 2020) and force the underlying current (Wu 1968; Lin *et al.* 2008; Wu & Deike 2021). With this widely adopted assumption (which we will test explicitly in this paper), the energy input rate can be written as (Grare *et al.* 2013)

$$S_{in} \approx \langle -p_s\boldsymbol{n}\cdot\boldsymbol{u_s}\rangle \approx c\langle p_s\frac{\partial h_w}{\partial x}\rangle \tag{1.1}$$

where S_{in} denotes the wave-averaged rate of energy input flux. The angular brackets denote averaging over one wavelength, and $\boldsymbol{u_s}$ is the surface water velocity. The part of $\boldsymbol{u_s}$ that is correlated to the pressure is by linear approximation the vertical wave orbital velocity $w_{orbit} = -c(\partial h_w/\partial x)$, with c the wave phase speed. Note that $\langle p_s\partial h_w/\partial x\rangle$ is the wave drag force F_p, similar to the concept of the form drag of a blunt body.

Based on (1.1), the key to determine the rate of energy input is the correlation between the surface pressure profile and the surface slope. Experimental measurements (Plant 1982; Peirson & Garcia 2008; Grare *et al.* 2013; Buckley *et al.* 2020; Funke *et al.* 2021) have directly or indirectly estimated this correlation (more on the experimental methods in §1.4). It is also a framework that most theoretical works have adapted.

1.3. *A brief review on the representation of surface pressure in wind wave growth theories*

We first present a brief review of some of the theories developed over the years to describe wind wave growth, and how they have affected the representation and comparison of experimental data.

Jeffreys (1925) was the earliest to propose what is now called the 'sheltering hypothesis', where the surface pressure is assumed to be 90° out of phase with the surface, i.e. in phase with the slope,

$$p_s = s_z \rho_a (U_z - c)^2 \frac{\partial h_w}{\partial x}, \tag{1.2}$$

where s_z is the sheltering coefficient, and U_z a reference velocity at a given height z. The choice of the reference velocity is not specified, and (1.2) can be interpreted as a scaling analysis. The energy input rate S_{in} follows (1.1) and reads

$$S_{in} = \frac{1}{2} \rho_a s_z (ak)^2 c (U_z - c)^2, \tag{1.3}$$

assuming that the surface elevation has the sinusoidal form $h_w = a\cos(kx)$. The viscous stress input was assumed to be negligible compared to the pressure input. Jeffrey's original idea is that the airflow is separated behind the wave crest, and therefore, his theory is not limited to small amplitude waves.

Miles (1957) proposed the critical layer theory through a linear stability analysis. The airflow is assumed to be inviscid and laminar, and as a result of that assumption, the forcing comes solely from the pressure. The shifted pressure profile is assumed the complex form

$$p_s = (\alpha + i\beta) \rho_a U_{ref}^2 k h_w \tag{1.4}$$

while the surface elevation h_w is

$$h_w = a e^{i(kx - \omega t)} \tag{1.5}$$

Again U_{ref} is an arbitrarily chosen reference velocity. The energy input, however, was not computed from (1.1), but from a change to the complex wave phase speed c through the boundary condition at the interface,

$$c = c_0 + \frac{1}{2} \frac{\rho_a}{\rho_w} (\alpha + i\beta) (U_{ref}/c_0)^2. \tag{1.6}$$

where c_0 is the phase speed of a free surface gravity wave. The wave energy rate of change dE/dt (or S_{in}) is normalised by the wave angular frequency ω and the wave energy E in order to yield the growth rate form of

$$\gamma = \frac{1}{\omega E} \frac{dE}{dt} = \frac{S_{in}}{\omega E} \approx 2\Im(c)/\Re(c) = \beta \frac{\rho_a}{\rho_w} \left(\frac{U_{ref}}{c} \right)^2, \tag{1.7}$$

neglecting wave dissipation by viscosity. In another word, the perturbation grows exponentially under the linear stability analysis, and finding the growth rate (per radian) γ is equivalent to finding β, the imaginary part of the surface pressure distribution. This requires solving the Rayleigh equation, and β was found to be related to the curvature of the mean wind velocity profile at the critical height (where the wind speed equals the wave phase speed).

The applicability of the critical layer theory has been questioned, as it ignores turbulence effects; for short and slow travelling waves, the critical layer is very close to the water surface (Belcher & Hunt 1993; Janssen 2004), where viscous effect might be

important; it also does not capture the effect of finite amplitude or steep waves (Peirson & Garcia 2008). As an improvement to Miles' theory, Belcher & Hunt (1993) and Belcher (1999) incorporated the turbulence's effects and proposed the non-separated sheltering mechanism. The turbulent boundary layer is divided into the inner surface layer, the stress surface layer, the middle layer and the outer layer based on the asymptotic structure of the flow. The surface pressure is

$$p_s = (-1 + i\frac{u_*^2}{U_m^2}\beta)\rho_a U_m^2 k h_w, \tag{1.8}$$

where U_m is the middle layer velocity, and β was attributed to a few different mechanisms. Since only the turbulent stress is considered, which goes to zero at the surface, the energy input is by construction only done by the surface pressure.

All the above theories have attributed the energy input to the surface pressure forcing. What 1.2, 1.4, 1.8 have in common is a phase shifted pressure profile, and the amplitude of the pressure profile given by ρ_a times some reference velocity U_{ref}^2 (1.2 can be written as $p_s = is_z\rho_a(U_z - c)^2 k h_w$, and the sheltering coefficient s_z is equivalent to β if $U_z - c = U_{ref}$). Understanding what controls the phase shift and the reference velocity in various regimes, however, is no easy work, and depends on the specific proposed mechanism, as well as the mean wind velocity profile.

1.4. *Connecting theoretical growth rate and observations*

Experimental measurements of the input rate S_{in} have followed different approaches. One option is to measure the correlation $\langle p_s \partial h_w/\partial x\rangle$ in 1.1 by simultaneous measurement of the pressure and the surface elevation (Snyder *et al.* 1981; Donelan *et al.* 2006; Grare *et al.* 2013). Directly measurement of the surface pressure requires complex wave following pressure sensors, which tend to be limited in responding frequencies, and have to be placed at a certain height above the water surface, which introduces additional uncertainty (Donelan *et al.* 2006; Grare 2009). Alternatively Buckley *et al.* (2020) performed PIV measurements of the air flow above the wave and estimated the pressure forcing as residual stress or from pressure reconstruction (Funke *et al.* 2021).

The other option is to directly measure the wave energy growth from temporal or spatial evolution of the surface elevation (Kawai 1979; Peirson & Garcia 2008). The wave energy rate of change is related to the energy input rate by

$$S_{in} = D + dE/dt, \tag{1.9}$$

where D is the wave dissipation term, usually estimated from the linear viscous dissipation rate (Lamb 1993)

$$D = 4\nu_w k^2 E \tag{1.10}$$

where $\nu_w = \mu_w/\rho_w$ is the kinematic water viscosity. The dissipation term D is small for relatively long waves above $O(1\text{m})$ but not negligible in some lab scale experiments. This method measures S_{in} without the assumption that the pressure forcing is the dominant contribution (Peirson & Garcia 2008). The difficulty then resides in measuring the small fraction of change in the wave amplitude given the small values of the wave growth due to the small density ratio ρ_a/ρ_w. Uncertainties in the dissipation rate also remains, due to the role of parasitic capillary waves or micro-breaking that can dominate over the viscous dissipation especially in finite amplitude cases (Grare *et al.* 2013).

The experimental and field measurements of the energy input rate S_{in} have shown a reasonable agreement with (1.7), adopting the air friction velocity u_* as the reference velocity (Plant 1982). The definition of u_* is based on the total downward momentum

transfer and carries some uncertainty itself. There are other choices of the reference velocity, and therefore other representations of γ. For example, Donelan *et al.* (2006) adopted the sheltering hypothesis and found that using the wind velocity at half the wavelength $U_{\lambda/2} - c$ in (1.3) best collapsed their data.

To summarise, the experimental uncertainties, together with the indirect nature of the estimations of the energy input rate make it difficult to directly verify a specific growth mechanism. A direct connection to the various theories would require knowledge of not just the wave-averaged quantity S_{in}, but also the phase resolved pressure profile p_s. Few experimental works (Donelan *et al.* (2006); Grare (2009) to our knowledge) have discussed the pressure profile itself, due to the difficulty of pressure measurement.

Numerical simulations have much to offer in this regard, and can focus on either the wind or the wave side. Simulations focused on the turbulent airflow over a wavy boundary (stationary or with prescribed wave motion) have been conducted using both direct numerical simulations (DNS) (e.g. Sullivan & McWilliams 2010; Kihara *et al.* 2007; Yang & Shen 2010) and large eddy simulation (LES) (e.g. Yang *et al.* 2013). They provide detailed information about the wave induced perturbation and stresses, and the wave growth is inferred from 1.1. DNS does not require subgrid scale models but is limited by the high computational cost associated with high Reynolds number. Wall modelled LES, on the other hand, is able to simulate much higher Reynolds number flows, but the subgrid scale models for wave drag is still under development (Deskos *et al.* 2021; Aiyer *et al.* 2021). Most importantly, wall modelled LES, by design, does not offer enough insight into the dynamics of wave growth since the wall models assume knowledge of this process (Piomelli & Balaras 2002). Wall resolved LES has been applied to the study of a broadband wave field growth (Yang *et al.* 2013), but it is also restricted in the Reynolds number similar to DNS. Simulations focused on the wave evolution usually simplify the wind effects into a forcing at the water top boundary, either as solely a phase-shifted pressure distribution (Fedorov & Melville 1998; Zdyrski & Feddersen 2020), or as both pressure and viscous shear stress distribution (Tsai *et al.* 2013). This requires the stress distribution as prior knowledge, which as we have discussed, is far from understood.

Almost the entirety of the numerical work has been limited to one side of the problem, and there has been very few numerical simulations of the fully coupled wind wave interaction. To our knowledge, the only numerical works where both the wind and the growth of the surface waves are directly resolved are in the context of the very initial wave generation (Lin *et al.* 2008; Li & Shen 2022).

What distinguishes this work from previous numerical works is therefore the fully-coupled approach. We extend our earlier 2D study with linear-shearing laminar wind forcing (Wu & Deike 2021) to a 3D turbulent boundary layer wind forcing. We use a volume of fluid (VoF) method to reconstruct the interface and access the wave growth, including the case of steep waves. We can access the wave growth from directly observable wave evolution, in addition to inferring it from the pressure-slope correlation. This allows us to verify the assumption (1.1) that S_{in} mostly results from the pressure stress. We also discuss the spatial structure of the pressure field and phase shift with the wave profile. We study independently the effects of two key parameters, the wave steepness ak and the ratio between the wave phase speed and the wind friction velocity c/u_* (referred to as wave age in wind wave literature). In experiments, the two parameters are connected by the fetch-limited relation, and therefore their respective effects are hard to separate.

The paper is structured as follows. In §2 we introduce the numerical setup. In §3 we define the wave averaged quantities of interests: the wave energy, and the momentum and energy fluxes. We cross-check the wave growth obtained from wave surface elevation and from the pressure-slope correlation. In §4 we present the surface pressure distribution

(phase shift and amplitude) for different $c/u*$ and ak values. In §5 we discuss the scaling of the wave drag force, and the energy input rate with c/u_* and ak. We compare with previous data sets and discuss the implications for possibly applicable theories.

2. Direct numerical simulation of fully coupled wind and waves

We present direct numerical simulations of fully coupled wind forced water waves. We solve the two-phase Navier-Stokes equations with the Basilisk solver (Popinet 2009, 2015, 2018; Fuster & Popinet 2018), with a momentum conserving scheme (Zhang *et al.* 2020) and a geometric volume of fluid (VoF) method to reconstruct the interface. We use adaptive mesh refinement (AMR) which allows us to reduce the computational cost when solving such a multi-scale problem. The methods have been extensively validated and applied to wave breaking (Deike *et al.* 2015, 2016; Mostert & Deike 2020; Mostert *et al.* 2022), two-phase turbulent flow (Rivière *et al.* 2021; Perrard *et al.* 2021; Farsoiya *et al.* 2021), and atmospheric turbulent boundary layer (van Hooft *et al.* 2018).

2.1. *Numerical setup*

The computation domain is of size $L_0 \times L_0 \times L_0$, with four waves in the x direction of wavelength $\lambda = L_0/4$ (wave number $k = 2\pi/\lambda = 8\pi/L_0$). The depth of the resting water is $H_w = L_0/2\pi$, while the height of the airflow is $H_a = L_0(1 - 1/2\pi)$ (see figure 2). The top and the bottom are both free slip boundary conditions, while the front and back, left and right are periodic boundary conditions.

The turbulent boundary layer and the waves are initialised independently. We force the turbulence with a pressure gradient (similar to a canonical channel flow), which sets the *nominal* friction velocity u_* (i.e. total wall stress τ_0)

$$\tau_0 = \rho_a u_*^2 = H_a \frac{\partial p}{\partial x}. \tag{2.1}$$

The friction Reynolds number is defined as

$$Re_* = \frac{\rho_a u_* H_a}{\mu_a}, \tag{2.2}$$

and set to 720 for all cases, defining the viscous length scale $\delta_\nu = \nu_a/u_* = H_a/720$. We have validated the solver against a canonical flat wall case with $Re_* = 180$ (Kim *et al.* 1987) (see appendix A for details). The mean wind velocity profile of such a channel flow follows the law of the wall, and is similar to that of laboratory wind wave experiments (e.g. Buckley *et al.* 2020).

The wave initial condition is given by a third order Stokes wave similar to Wu & Deike (2021), with initial steepness ak. It is kept stationary until the turbulence reaches a statistical steady state. Then, the wave is released at $t = 0$, travelling with a phase speed given by the free surface dispersion relation

$$c = \sqrt{g/k + \sigma k/\rho_w}, \tag{2.3}$$

where g is the gravitational acceleration and σ is the surface tension. The orbital velocity is initialised with the corresponding velocity field of the third order Stokes wave (see Wu & Deike 2021).

Since we initialise the waves with a solution of the free surface gravity wave equation, we expect the flow field to self-adjust under wind forcing during the very early stage of the simulation. The turbulent boundary layer also goes through a relaxation period when the near-wall flow adjusts to the moving boundary. Therefore, the first two wave periods

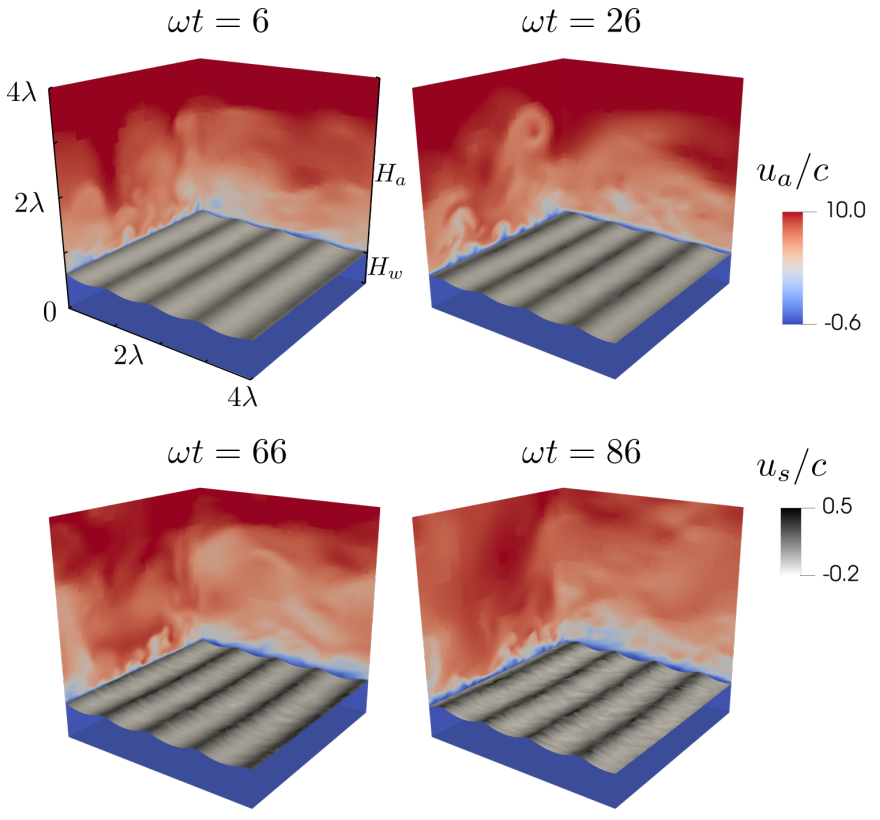

FIGURE 2. Snapshots of wave growth. There are four waves in the computational domain, and the height of the water and the half channel height for the air are shown. The colours indicate the instantaneous horizontal wind velocity, and the surface water velocity, respectively. The waves grow in amplitude and become short crested, a characteristic of wind waves. At later stage, the waves also appear to be three-dimensional because of the development of an underwater turbulent boundary layer, although any 3D effects are not discussed in the current paper.

are not considered in the data analysis. Since the wave period $T = 2\pi/\omega$ is very large compared to the inner turbulent time scale $t_\nu = \nu_a/u_*^2$, it is enough time for the near wall turbulence to reach equilibrium with the moving waves. The equilibrium is also checked by examining the mean velocity profiles. After that, the waves and the turbulence interact in a fully coupled way without any prescribed interfacial conditions. We note that the whole simulation is transient by nature, meaning that the wave amplitude changes with time, despite over a much longer time scale than both the turbulence time scale and the wave period.

The non-dimensional numbers relevant for the waves are

$$Bo = \frac{(\rho_w - \rho_a)g}{\sigma k^2}, \quad Re_w = \frac{\rho_w c \lambda}{\mu_w}. \tag{2.4}$$

In all the cases presented in this paper, the Bond number $Bo = 200$ so that the waves are in the gravity wave regime, and we have verified that further increasing Bo does not affect the results presented here (see appendix A). The density ratio ρ_a/ρ_w is set to air-water conditions 1/850, while the viscosity ratio μ_a/μ_w is always larger than 50 and is adjusted to set the air friction Reynolds number Re_* (2.2) and the wave Reynolds

ak	c/u_*	$k\delta_\nu$*	kl_c	a/Δ	δ_ν/Δ	$k\Delta$
0.10	2,4,6,8			4.1		
0.15	2,3,4,6,8	0.029	0.44	6.1	1.2	0.025
0.20	2,4,6,8			8.1		
0.25	2,4,6,8			10.2		

TABLE 1. A table of controlling parameters ak and c/u_*, and relevant length scales. The third and fourth columns are the viscous wall unit $\delta_\nu = \nu_a/u_*$ and the capillary length scale $l_c = 2\pi\sqrt{\sigma/(\rho_w - \rho_a)g}$ relative to $1/k$ respectively, showing the physical relevance of the parameters. They are controlled by $\mathrm{Re}_* = 720$ and $\mathrm{Bo} = 200$ and kept constant. The last three columns are a, δ_ν and k relative to the smallest grid size Δ, showing the numerical resolution. In the simulations, $\Delta = L_0/2^N$, where $N = 10$ is the maximum refinement level of the octree adaptive grid. *For wall modelled LES, the roughness length kz_0 is usually reported instead of $k\delta_\nu$. If we use the $z_0 = 0.11\nu_a/u_* = 0.11\delta_\nu$ conversion for flat smooth surface, $kz_0 = 0.003$. Also notice that these length scale are not changed when we change c/u_* because k is fixed, in contrast to the realistic situation, where wave number k is smaller for fast moving waves.

number Re_w (2.4) independently. The wave Reynolds number is kept at $Re_w \approx 10^5$. Note that the value of Re_w gives the linear dissipation rate (per radian) due to viscosity γ_d

$$\gamma_d = -4\nu_w k^2/\omega = \frac{8\pi ck}{Re_w}/\omega = 8\pi/Re_w \tag{2.5}$$

and $D = \gamma_d \omega E$ (equivalent to 1.10).

Notice that the velocity ratio (wave age) c/u_* is varied by changing c, while keeping u_* constant, independently of the steepness ak. This configuration allows to resolve the turbulent air flow and capture the wave growth for c/u_* ranging from 2 to 8 and ak from 0.1 to 0.25. Table 1 summarizes the simulation conditions, together with the characteristic length scales of the turbulence δ_ν and the capillary length l_c, relative to wave number k and to the smallest grid size Δ.

3. Direct observation of the wind wave growth and the surface stress

3.1. *Directly observed wave growth*

Figure 2 shows the wave surface evolving due to the turbulence forcing, with growth and steepening as the wind keeps blowing. The waves can be considered approximately monochromatic in the simulation, since the development of higher frequency ripples and 3D structure do not occur until later stage, and the downshift of peak frequency is constrained by the periodic boundary condition. However, the wave shape changes and becomes short-crested, which is a feature of wind waves. We quantify the growth of the waves through the time evolution of the water surface elevation $h_w(x, y, t)$, which we use to directly compute the wave energy (neglecting the surface tension energy):

$$E_{rms}(t) = \rho_w g \langle h_w^2(x, y, t) \rangle. \tag{3.1}$$

with the spatial wave averaging of a quantity q, in the $x - y$ plane, being defined as

$$\langle q \rangle = \frac{1}{L_0^2} \int_{-L_0/2}^{L_0/2} \int_{-L_0/2}^{L_0/2} q \, dxdy \tag{3.2}$$

Figure 3 shows the time evolution of $E_{rms}(t)$ for three different c/u_* cases, with initial wave steepness $ak = 0.2$. The smallest wave age case has the strongest wind forcing, and therefore the largest growth rate. The $c/u_* = 8$ case presents an almost exact balance

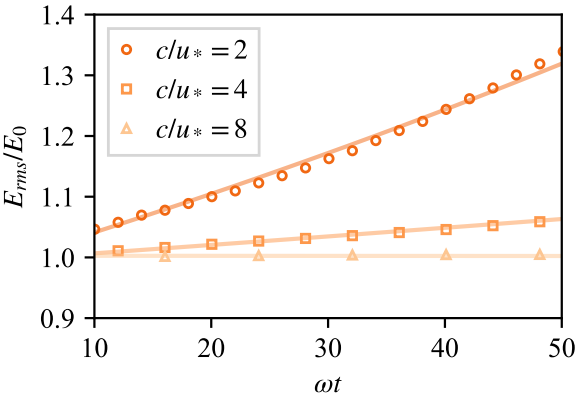

FIGURE 3. Wave energy normalised by initial energy $E_0 \equiv E_{rms}(t=0)$, as a function of time, directly computed from water surface height output $h_w(x, y, t)$, for three different wave c/u_* = 2,4,8, and initial steepness $ak = 0.2$. The solid curves are exponential fits to the points, although we caution that the growth rates are so small that for the exponential growth cannot be distinguished definitively from a linear growth. The $c/u_* = 2$ case grows the fastest while the $c/u_* = 8$ case is very slowly decaying. Note that both E_0 and ω change with c/u_* because g is changed in the numerical setup (see §2).

between the wind input and viscous dissipation, resulting in a nearly constant wave energy with time. From this directly observed wave growth, we can measure a temporal rate of change of energy dE/dt (here after we omit the subscript rms for brevity). The wave growth is rather slow, and happens over $O(10)$ wave periods and $O(100)$ to $O(1000)$ turbulent time scale t_ν. This slow change in the wave energy is related to the small density ratio ρ_a/ρ_w, which implies weak air-water coupling; see (1.7).

3.2. *Wind surface stress*

Apart from the direct surface elevation h_w, we extract the surface stress from the simulation. The wind stress *at the surface* consists of two parts, the pressure variation $\boldsymbol{\tau_p}$ (i.e. drag force) and the viscous stress $\boldsymbol{\tau_\nu}$ (see Grare *et al.* 2013; Peirson & Garcia 2008):

$$\boldsymbol{\tau_p} = -p_s \boldsymbol{n}, \quad \boldsymbol{\tau_\nu} = \mu_a(\boldsymbol{\nabla u_a} + \boldsymbol{\nabla u_a}^T)\boldsymbol{n} = (\tau_{\nu x}, \tau_{\nu y}, \tau_{\nu z}) \tag{3.3}$$

where $\boldsymbol{u_a}$ is the air velocity vector, p_s is the surface pressure, $\boldsymbol{n}$ is the normal vector of the water surface.

Figure 4 shows the instantaneous stress fields projected onto a wave following surface very close (4Δ) to the water surface. Since the plane is in the viscous sublayer, it is considered close enough to the actual surface that the turbulent stress can be ignored. Both the pressure and the shear stress present clear wave coherent patterns, while also having 3D structures due to the turbulence. For example, the streaks shown in figure 4(b) are about $100\delta_\nu$ apart, which is consistent with the typical structure of wall bounded turbulent flows. There is an-order-of-magnitude difference between the pressure and shear stress (but not their horizontal projection in (3.4)). The maximum of the pressure appears on the windward face, which is left to the grey line indicating the wave crest in figure 4; this gives rise to the non-zero correlation in (1.1). The viscous shear stress also reaches maximum near the wave crest due to the straining of the shear layer.

From the stress field we can compute the wave averaged integral quantities: the momentum flux (total stress τ_{total}) and the energy flux (input rate S_{total}). The total

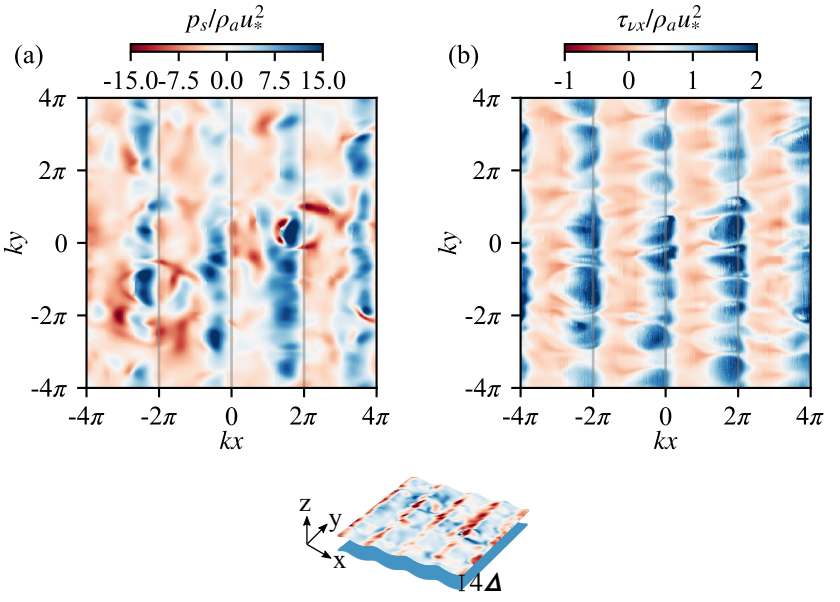

FIGURE 4. Instantaneous pressure (a) and the horizontal component of viscous stress (b) projected onto the wave following surface $4\Delta = 0.1/k$ above the water surface, at $\omega t = 38$, for the case of $c/u_* = 2$ and $a_0 k = 0.2$. Notice that there is one order of magnitude difference in the colour scale range. The grey lines show where the wave crests are. There are clearly wave coherent patterns.

horizontal wind stress

$$\tau_{total} = \langle \boldsymbol{\tau_p} \cdot \boldsymbol{e_x} \rangle + \langle \boldsymbol{\tau_\nu} \cdot \boldsymbol{e_x} \rangle = \langle p_s \frac{\partial h_w}{\partial x} \rangle + \langle \tau_{\nu x} \rangle \equiv F_p + F_s, \tag{3.4}$$

is the sum of the form drag force per unit area F_p and the averaged viscous stress in the horizontal direction F_s. Notice that the linear approximation ($d\eta/dx \ll 1$) is considered.

This stress (momentum) partition is closely related to, but different from the energy input partition. The total energy input rate by the wind stress (into *both* waves and underwater drift layer) is a product of the stress and the surface water velocity

$$S_{total} = \langle \boldsymbol{\tau_{total}} \cdot \boldsymbol{u_s} \rangle = \langle -p\boldsymbol{n} \cdot \boldsymbol{u_s} \rangle + \langle \boldsymbol{\tau_\nu} \cdot \boldsymbol{u_s} \rangle \equiv S_p + S_s. \tag{3.5}$$

The part of $\boldsymbol{u_s}$ that correlates with the pressure is the vertical orbital velocity w_{orbit}, which gives (1.1); the part of $\boldsymbol{u_s}$ that correlates with the viscous stress, however, contains both the wave horizontal orbital velocity u_{orbit} and the drift velocity u_d:

$$S_s = \langle \boldsymbol{\tau_\nu} \cdot \boldsymbol{u_s} \rangle \approx \langle \tau_{\nu x} u_{sx} \rangle = \langle \tau_{\nu x} u_{orbit} \rangle + \langle \tau_{\nu x} u_d \rangle \equiv S_{s,w} + S_{s,d}, \tag{3.6}$$

where $S_{s,w}$ and $S_{s,d}$ denote the energy input by the viscous shear stress into the waves and the drift respectively. The development of the drift is discussed in Wu & Deike (2021), and here we focus on the energy input into the waves

$$S_{in} = S_p + S_{s,w} = c\langle p_s \frac{\partial h_w}{\partial x} \rangle + \langle \tau_{\nu x} u_{orbit} \rangle. \tag{3.7}$$

Notice that the assumption $S_p = cF_p$ means that the pressure induced form drag contributes solely to the wave growth, while only a small variation of the viscous shear stress is correlated with u_{orbit} and can contribute to the wave growth (Peirson & Garcia 2008). In other words, it is not the mean stresses but the correlated part of the stresses

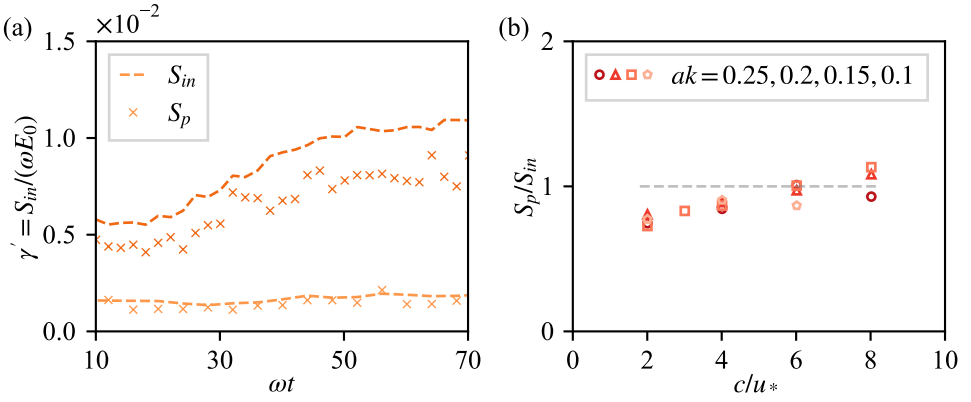

FIGURE 5. (a) The instantaneous pressure energy input rate $S_p = cF_p = c\langle p_s \partial h_w/\partial x\rangle$ closely follows the instantaneous wave energy growth rate (corrected with dissipation) $S_{in} = dE/dt + D$ for $c/u_* = 2$ (dark orange) and $c/u_* = 4$ (light orange); both are of $ak = 0.2$. The curves are smoothed out using a moving window averaging. The variation in S_p is mostly due to turbulence fluctuation. (b) The ratio between the averaged pressure energy input rate S_p and the total input rate $S_{in} = (E(t_1) - E(t_2))/(t_1 - t_2) + D$ computed over 10 wave periods. The ratio stays close to 1 for all the simulation cases with some variations.

with the *wave* surface velocity that contributes to the wave energy growth. In reality, F_p and F_s are of the same order of magnitude, but S_p is generally thought to play a dominant role over $S_{s,w}$ (i.e. $S_{in} \approx S_p$), as mentioned in the introduction. We will examine both the momentum and the energy partitions using the simulation data.

In this paper we refer to the form drag F_p as the wave drag force, and drag coefficient as the ratio F_p/τ_{total}. Note that the wave drag force in the literature sometimes refers to the effective stress that contributes to the wave growth (from the energy flux S_{in}, instead of the momentum flux partition), and includes the pressure and the wave coherent viscous stress (Peirson & Garcia 2008; Grare *et al.* 2013; Melville & Fedorov 2015; Buckley *et al.* 2020, etc.),

$$\tau_w = S_{in}/c = F_p + S_{w,s}/c. \tag{3.8}$$

3.3. *Wave energy growth rate vs pressure input rate*

The direct wave growth and surface stress extracted from the simulation and introduced in §3 offer two ways of computing the energy input rate into the wave S_{in}. First, we compute dE/dt from figure 3 and correct for the dissipation (1.9); and second we extract the surface pressure p_s and compute the correlation (1.1).

Figure 5(a) shows a comparison of the results obtained using the two methods. The wind input rate $S_{in}(t)$ computed with (1.10) is plotted with dotted lines, and the pressure input rate $S_p(t)$ computed with (1.1) is with crosses, for $c/u_* = 2$ and 4. In both cases, the pressure input S_p closely follows the wave energy growth rate S_{in}, although there is a small gap for the $c/u_* = 2$ case. A further demonstration of the dominant role of the pressure term is shown in figure 5(b), where we plot the ratio S_p/S_{in} averaged over 10 wave periods for all the cases. The ratio is very close to 1 for most cases, indicating that the pressure input S_p is the major energy input term in S_{in}. Again, the smallest wave age cases ($c/u_* = 2$) present the largest difference ($S_p/S_{in} = 0.8$) and indicate that the wave coherent viscous stress might start to play a role in the strongly forced cases.

Note that at high c/u_*, uncertainties in the budget are related to uncertainties of the decay rate for finite amplitude waves, which get amplified by the large E for the

fast travelling waves, together with the very small decay rate which are also hard to accurately capture numerically. Furthermore, the viscous stress input S_s could potentially be negative for these fast travelling cases.

We want to point out that the dissipation correction is necessary in our cases, as the dissipation is non-negligible due to the limited Re_w. Although the wave Reynolds number Re_w is constant (and therefore γ_d is the same for different cases by (2.5)), we still have different values of D for different cases of different wave frequency ω and initial energy E_0. The faster travelling waves have higher E_0 and therefore higher D, and the relative change in energy is much smaller. This relative change in energy (per radian) is reflected by the parameter γ (defined in 1.7). The underlying assumption of (1.7) is that the wave growth is exponential, and γ represents the exponential growth rate per radian. In our simulations, we find that the growth rates are so small that for most cases, this exponential growth cannot be distinguished from a linear growth, and the growth rate computed by $\gamma' = S_{in}/(\omega E_0)$ shows more directly the trend of S_{in}. There is an uptake of S_{in} as the instantaneous amplitude slowly increase over the interval of about 10 wave periods for the $c/u_* = 2$ case; in contrast, S_{in} stays almost constant for the $c/u_* = 4$ case, as the amplitude growth is so small that its effect on S_{in} is negligible.

The analysis above involves wave averaged quantities (S_p, E, etc.), and overall, S_p does plays a dominant role in wave growth.

4. Surface pressure distribution

4.1. *Definitions*

We now analyse the detailed structure of the surface pressure distribution p_s relative to h_w, as it reveals the dynamics of the wind wave interaction. The structure of the pressure field is shown in figure 4(a) and clearly contains wave-induced signals, while also being influenced by the instantaneous turbulence. To distinguish the wave-induced effect from the turbulent fluctuation, we introduce phase averaging. For any quantity $q(x, y, z)$, the phase average is

$$\bar{q}(\theta, z) = \frac{1}{N_{\mathrm{w}} L_0} \sum_{n=1}^{N_{\mathrm{w}}-1} \int_{-L_0/2}^{L_0/2} dy\, q(x = \lambda(n + \theta/2\pi), y, z), \tag{4.1}$$

where $\lambda = 2\pi/k = L_0/4$ is the wavelength of the initial waves, and $N_{\mathrm{w}} = 4$ is the number of waves in the x direction. The phase θ can be extracted from the surface elevation $h_w(x, y, t)$ and is therefore generalizable to cases which are not strictly sinusoidal.

The surface pressure can be generally described as the sum of different frequency modes,

$$p_s(\theta, t) = \sum_{n=1}^{\infty} \hat{p}_n \cos(n\theta + \phi_{pn}) \tag{4.2}$$

where ϕ_{pn} is the pressure phase shift and $\hat{p}_n$ is the pressure amplitude of mode n. Meanwhile, the surface elevation can be written as

$$h_w(\theta, t) = \sum_{n=1}^{\infty} a_n \cos(n\theta + \phi_n), \tag{4.3}$$

with $h_w(\theta, t) \approx a\cos(\theta)$ since the surface elevation h_w is largely monochromatic in our simulation (and we can always shift the reference point so that the phase ϕ_1 is zero).

Once given the surface pressure distribution p_s (4.2), the wave drag force F_p (3.4)

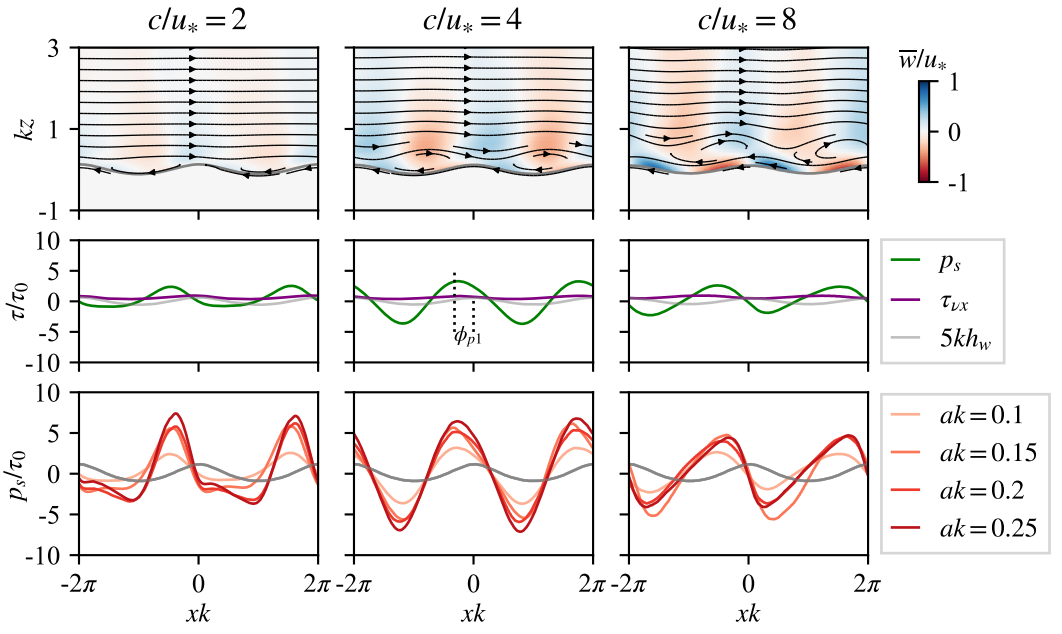

FIGURE 6. Vertical velocity field, streamline and 1D stress distribution for three different wave ages $c/u_* = 2, 4, 8$. Top row: solid black lines in the top row are streamlines in the moving wave frame of reference (i.e. plotted with $\bar{w}$ and $\bar{u} - c$), and the colour shows the phase averaged vertical velocity $\bar{w}$. Notice that the higher the c/u_*, the further the wave induced perturbation extends above the waves. Middle row: The asymmetric pressure distributions (green lines) that result from the distorted streamlines. The purple line is the shear stress. $ak = 0.1$. The phase shift ϕ_p between the pressure p_s and the water surface elevation h_w gives rise to the drag force and energy input. Bottom row: the shape of the p_s distribution is consistent across different steepness, shown by different colours. The amplitude, however, seems to increase from low ($ak = 0.1$) to moderate ($ak = 0.15$) steepness, but not change much from moderate to high steepness ($ak = 0.2, 0.25$). The grey lines in all plots indicate the wave surface position, with exaggerated steepness.

becomes

$$F_p = \langle p_s \frac{\partial h_w}{\partial x} \rangle \approx \sum_{n=1}^{\infty} \hat{p}_n \, a_n nk \langle \cos(n\theta + \phi_{pn}) \sin(n\theta + \phi_n) \rangle \tag{4.4}$$

$$= \hat{p}_1 \, ak \langle \cos(\theta + \phi_{p1}) \sin(\theta) \rangle = \frac{1}{2} \, ak \, \hat{p}_1 \sin(\phi_{p1}), \tag{4.5}$$

and S_p follows as $S_p = cF_p$. Finding the drag force and the pressure input rate now simplifies to finding the pressure perturbation amplitude $\hat{p}_1$ and the phase shift ϕ_{p1} that correspond to wave number k. Notice how a non-zero phase shift ϕ_p is necessary for a non-zero F_p and S_p. Since (4.4) shows that only the principal mode ($n = 1$) contributes to the wave growth, we then focus on how $\hat{p}_1$ and ϕ_{p1} depend on c/u_* and ak qualitatively.

4.2. *Streamline and asymmetric pressure patterns*

Figure 6 top row shows the phase averaged vertical velocity $\bar{w}$, for three flow conditions (c/u_*=2,4,8; ak=0.1). The alternating patterns demonstrate the perturbation by the waves, as opposed to uniform zero for a flat surface. In the slowest wave cases (i.e. $c/u_* = 2$), the alternating sign mostly comes from the straining and relaxing of the shear layer

(because the airflow follows the boundary shape). In the intermediate wave speed cases ($c/u_* = 4$ and 8), the wave orbital velocity becomes significant and it leaves an imprint on the airflow (because the airflow follows the vertical motion of the boundary). Here we are plotting below $kz = 3$, however we noticed that the wave induced perturbation in $\bar{w}$ extends higher up with increasing c/u_*, to almost $kz = 2\pi$, in the $c/u_* = 8$ case.

In figure 6 top row we also plot the streamlines in the wave frame of reference (i.e with $\bar{w}$ and $\bar{u} - c$). There are recirculation cells because the vertical velocity is of alternating signs, and the horizontal velocity changes sign at some height. This height is often called the critical height, and it depends on the value of c/u_*. The higher c/u_* is, the further away the critical height is from the water surface. These recirculating cells generate the pressure variation p_s at the water surface, plotted in the middle row of figure 6 with green lines.

The middle row of figure 6 is the averaged stress distribution for both the pressure and the viscous shear stress (shown in fig. 4). We see clearly that the pressure maximum is on the windward face, and the phase shift is marked by ϕ_{p1}. Notice that even for the smallest steepness case ($ak = 0.1$), the shapes of the pressure distribution are not sinusoidal. For example, at $c/u_* = 2$, the trough of the pressure signal is rather flat, which is a sign of a certain level of flow separation or non-separated sheltering. For the $c/u_* = 8$ cases, the pressure distribution is tilted forward. Only in the $c/u_* = 4$ case does the pressure distribution roughly resembles a sinusoidal wave. The pressure structures are in qualitative agreement with those found in simulations (Yang & Shen 2010; Kihara *et al.* 2007) and experiments (Mastenbroek *et al.* 1996) with corresponding c/u_*. The non-sinusoidal pressure shape is the signature of higher frequency modes and would contribute to the growth of corresponding wave frequencies.

The bottom row shows how the 1D pressure distribution changes with different ak, ranging from 0.1 to 0.25 (colour coded). The shapes are similar for the same c/u_*, with the amplitude of the pressure variation increasing with wave steepness ak. The largest difference is between $ak = 0.1$ and the other three ak values, where the amplitude of the pressure seems to saturate at high ak.

4.3. *Pressure amplitude and phase shift*

Figure 7 shows the pressure amplitude $\hat{p}_1$ and phase shift ϕ_{p1} as a function of c/u_* and ak. These quantities are computed by Fourier transform of the phase averaged surface pressure p_s. The 'surface' is defined as the wave following surface $4\Delta = 0.1/k$ away from the air water interface. We have tested the sensitivity to the location within the first 8 grid points and it does not present much difference (as long as we are in the viscous layer).

Figure 7(a) shows that the amplitude $\hat{p}_1$ first increases with c/u_* until $c/u_* \approx 6$ and then decreases, for all steepness ak. Figure 7(b) shows that the phase shift ϕ_{p1} follows the opposite trend. The net result is that the the drag force shown in figure 7(c) is not a strong function of c/u_*, which is in agreement with previous studies in the slow wave regime. Figure 7(c) also confirms (4.4): the dotted and solid lines show the single mode representation and the integral representation of wave drag force F_p respectively, which agree very well, even when the pressure distribution is not necessarily sinusoidal.

Taking a closer look at the phase shift, it is around 90 degree for the strongest forcing cases $c/u_* = 2$, and then goes under 90 degree between $c/u_* = 2$ and 6, and then slightly above 90 degree at $c/u_* = 8$. This indicates that the sheltering mechanism is dominant in the strong forcing conditions, and that the theories based on linear stability analysis might be at work in the higher wave age cases. (more on this in §5.3). Good agreement was found with results from Kihara *et al.* (2007) (marked with black crosses) at $ak = 0.1$

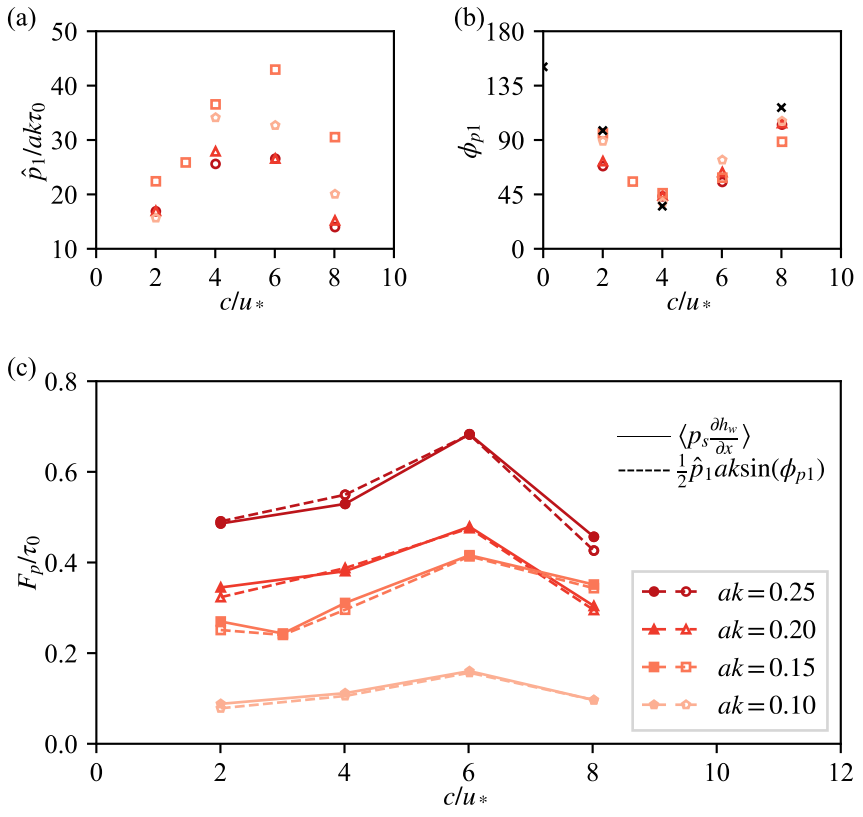

FIGURE 7. (a): Pressure amplitude $\hat{p}_1$ normalised by the nominal wall stress $\tau_0 = \rho_a u_*^2$, and in addition ak, plotted against c/u_*. (b): Pressure phase shift ϕ_{p1} as a function of c/u_*. Notice that because of the $F_p = (1/2)\hat{p}_1\, ak \sin(\phi_{p1})$ relation, the drag force is the largest when $\phi_p = 90^\circ$, and zero when $\phi_p = 0^\circ$ or 180°. The results of Kihara *et al.* (2007) of $Re_* = 180$ and $ak = 0.1$ are plotted with black crosses. (c)The wave drag force F_p is not a strong function of c/u_* for all the steepness ak. We also show the full integral value $\langle p_s \partial h_w/\partial x \rangle$ in comparison to the single mode representation $(1/2)\hat{p}_1 ak \sin(\phi_{p1})$. The markers and colours are the same with those in figure 5(b) and 6.

obtained at $Re_* = 180$, suggesting that the phase shift might not be sensitive to the Reynolds number.

The pressure amplitude $\hat{p}_1$ is normalised by $ak\tau_0$ in figure 7(a), and this choice is made by a commonly adopted scaling argument. Intuitively, and also used in the theoretical studies mentioned in §1.3, the pressure variation amplitude should scale with $\rho_a(ak)U_{ref}^2$ (1.4), with U_{ref} being some characteristic wind velocity (not necessarily the friction velocity u_*). From figure 7(a) we see that this scaling does not collapse $\hat{p}_1$ with respect to ak, at least not when u_* is used. Now defining the ratio between $\hat{p}_1$ and $ak\rho_a u_*^2$ as P,

$$P = \hat{p}_1/ak\rho_a u_*^2. \tag{4.6}$$

This ratio P represents $(U_{ref}/u_*)^2$, the ratio between the should-be characteristic velocity U_{ref} and the friction velocity u_*. From figure 7 (a) we see that P ranges from around 15 to 45, indicating that U_{ref}/u_* is around 4 to 7.

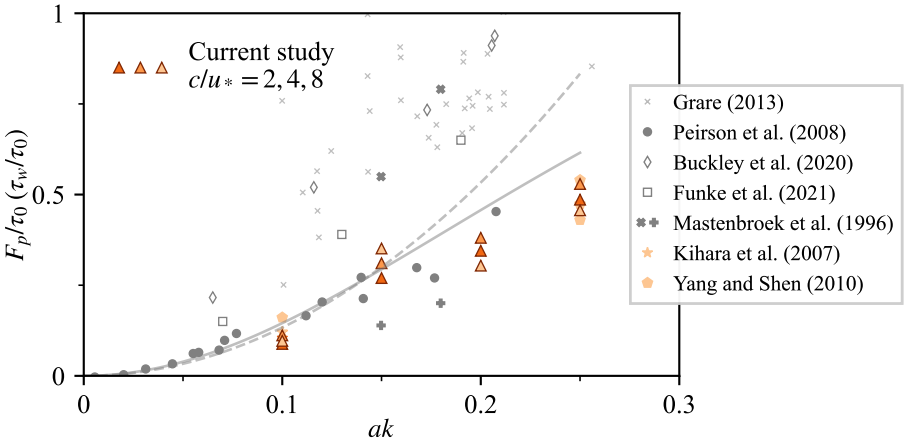

FIGURE 8. The wave form drag F_p (or wave drag τ_w defined by 3.8) as a proportion of the total stress τ_0, plotted as a function of wave steepness ak. Our data points are marked with the solid triangles and the colours denote c/u_*. Other numerical data: stars Kihara *et al.* (2007), $c/u_* = 2, 4, 8$, mostly overlapping with the $ak = 0.1$ results; pentagons, Yang & Shen (2010), $c/u_* = 2$. Experimental results: solid circles, Peirson & Garcia (2008); solid crosses, experimental observation from Mastenbroek *et al.* (1996); plus signs, numerical prediction from Mastenbroek *et al.* (1996); light crosses, Grare *et al.* (2013); open diamond, Buckley *et al.* (2020); open squares, Funke *et al.* (2021). The last two data sets denoted with open marks are purely wind generated waves, and the Grare *et al.* (2013) data set has mixed types, while the others are all mechanically generated waves (or similar numerical setups). Dashed line: the quadratic representation $F_p = 1/2\beta(ak)^2$ with a constant β; solid line: the Belcher correction 5.2.

5. Scaling the wave drag force F_p and the energy input rate S_{in}

In this section, we discuss the parameterization of the wave drag force F_p and the energy input rate S_{in} as functions of c/u_* and ak, and compare our results to those from the literature.

5.1. *Wave drag* F_p/τ_0

We have shown that the drag is not a strong function of c/u_* in the slow wave regime. However, it is strongly dependent on the steepness. Figure 8 shows the drag coefficient F_p/τ_0 as a function of the wave steepness ak. Since the amplitude changes very slowly in most cases, the initial steepness is a good enough representation of the transient $a(t)k$. For the small steepness regime ($ak < 0.2$), the data roughly scales with $(ak)^2$, with some small variation in different c/u_*,

$$F_p \sim (ak)^2 \tau_0. \tag{5.1}$$

More specifically the prefactor is $1/2P\sin(\phi_p)$, with P defined in 4.6. For higher steepness $ak = 0.2, 0.25$, we see a plateau in F_p/τ_0 and a clear departure from the $(ak)^2$ scaling, and slightly larger variation with c/u_*. This plateau is very likely due to the fact that the flow is mostly separated.

Figure 8 also shows numerical and experimental data from the literature. Our results agree very well with previous numerical studies across different ak. The $ak = 0.1$ results is very close to those from Kihara *et al.* (2007), and the $ak = 0.25$ results are within the range of those reported by Yang & Shen (2010). Note that Kihara *et al.* (2007); Yang & Shen (2010) performed DNS with $Re_* = 180$, which is four times smaller than

the current study. It suggests that the F_p/τ_0 as a function of ak may not be strongly Reynolds number dependent.

For comparison with experimental studies, we note that some of the data plotted in figure 8 are actually τ_w defined by (3.8) instead of F_p. Since we have already verified that the pressure is responsible for over 80% of the energy flux, the F_p and τ_w values do not differ by much for the cases discussed here; at least the small difference does not affect the general trend of F_p/τ_0 with increasing ak.

Peirson & Garcia (2008) (solid circles) measured τ_w by the spatial wave energy growth, and their data match with ours quite well. They also suggested a correction to the $(ak)^2$ relation inspired by (Belcher 1999), with two fitted parameters β_f and β_t

$$\tau_w/\tau_0 = (\beta_f + \beta_t)(ak)^2/[2 + \beta_f(ak)^2] \tag{5.2}$$

that seem to fit a compilation of the data sets well (see their figure 5). This correction is plotted with the solid line in figure 8. The other experimental studies have reported a wave drag coefficient somewhat higher. Mastenbroek *et al.* (1996) measured the wave drag coefficient by using a fixed pressure probe at a fixed height $kh = \pi$, and Grare *et al.* (2013) used PIV viscous stress measurement, pressure with fixed or wave following probe for different subset data. Buckley *et al.* (2020) and Funke *et al.* (2021) were obtained from the same data set; Buckley *et al.* (2020) used PIV viscous stress measurement and computed pressure as a stress residual, while Funke *et al.* (2021) reconstructed the pressure field by solving the Poisson equation.

From the synthesis of data, we can see that the numerical estimations of F_p/τ_0 are in general lower than the experimental measured ones; and that the ones inferred from the wave growth seem to be lower than the ones measured from the air stress in experiments. There are also significant scatters within experimental data using different methods to measure the stress (PIV viscous stress, pressure with fixed or moving probes), that are beyond the scatters that might be introduced by different wave ages. Although we have verified using our simulation that the measurement of F_p directly from the air stress or indirectly from the wave growth should be consistent, there remain a few possible reasons for the scatters in the experimental data: one is the existence of 3D smaller scale waves (roughness elements) that increases the drag; the other is the uncertainty caused by the air side measurement, especially the pressure extrapolation error from a finite height to the surface, discussed in Donelan *et al.* (2006) and Grare *et al.* (2013). A further examination of the extrapolation error will require a study of the vertical pressure structure.

5.2. *Growth rate* γ

The energy input by pressure is closely linked to the wave drag force by $S_p = cF_p$; or considering the more general definition of wave drag (3.8), the total wind input is $S_{in} = c\tau_w$. The two are used interchangeably in the present discussion, i.e. $S_{in} = c\tau_w \approx cF_p$.

We have seen that the drag force F_p is not a strong function of c/u_*, so the pressure energy input rate $S_p = cF_p$ increases with c/u_* as shown in the inset of figure 9, i.e. in the slow wave regime, the energy flux is higher for waves travelling faster (at a fixed u_*). This could appear in contradiction to the observation that the slowest travelling waves have the fastest growing energy curve in figure 3. This is however not self-contradicting, because the curves in figure 3 reflect the *relative* rate of change of energy, which is S_{in} further normalised by the total energy E, and E is larger for faster waves. (Note that in figure 3, since we consider the net energy growth, another factor that is the viscous decay is also larger for the faster waves, since γ_d is constant in our simulation).

This normalisation by the total energy E and angular frequency ω, i.e. the definition

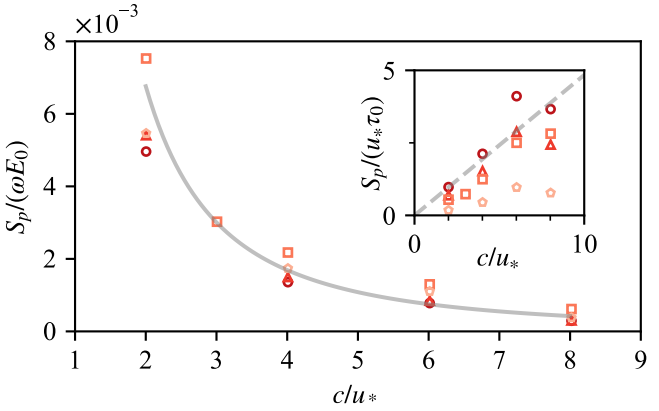

FIGURE 9. Inset figure shows the energy input rate S_p increasing with increasing c, while the main plot shows the non-dimensional growth rate (γ) decreasing with increasing c/u_*. The grey line is the $(u_*/c)^2$ fitting. It demonstrates that the non-dimensional growth rate scaling is dominated by the ωE normalisation.

of growth rate per radian $\gamma = S_{in}/(\omega E)$, was introduced by Miles (1957), and is based on the assumption that the growth is exponential. Considering the definitions of wave energy and the gravity wave dispersion relation,

$$E = \frac{1}{2}\rho_w g a^2, \quad \omega = kc = \sqrt{gk} \tag{5.3}$$

and using the assumption that $F_p \sim (ak)^2$ (which we have seen to be failing at high ak), and by introducing the prefactor β (Miles 1957), we obtain

$$F_p = \frac{1}{2}\beta(ak)^2\tau_0 = \frac{1}{2}\beta(ak)^2\rho_a u_*^2, \tag{5.4}$$

which becomes

$$\gamma = \frac{S_{in}}{\omega E} = \frac{cF_p}{\omega E} = \beta\frac{\rho_a}{\rho_w}\left(\frac{u_*}{c}\right)^2. \tag{5.5}$$

It is worth noticing that this relationship, widely used in the literature, presents some strong self-correlation between the normalisation of S_{in} by ω in the left hand side and the phase speed $c = \omega/k$ on the right hand side. The resulting $(u_*/c)^2$ scaling is reflected in figure 9.

The representation of (5.5) in figure 10 is often taken as an indirect proof of Miles' theory. Plant (1982) compiled laboratory and field measurements known to the date (plotted in grey symbols in figure 10), which became the benchmark and established the $(u_*/c)^2$ scaling, although the empirical range of β (indicated in grey dotted lines) is higher than the original prediction from Miles (1957).

We caution that while the $(u_*/c)^2$ scaling seems to hold, there is a wide scatter in the β value at a given value of u_*/c, with sometimes over an order of magnitude variation. We also note that alternatives for the reference velocity have been proposed (e.g. the sheltering coefficient at half wavelength by Donelan *et al.* (2006) or the middle layer velocity from Belcher (1999)), and the reported values of the β parameter by experimental and numerical studies could be presented in terms of another reference velocity, leading to estimations of the sheltering coefficient (see Peirson & Garcia (2008) and Yang *et al.* (2013) for example).

A large contributing factor to the scatter is the role of the wave steepness at a given

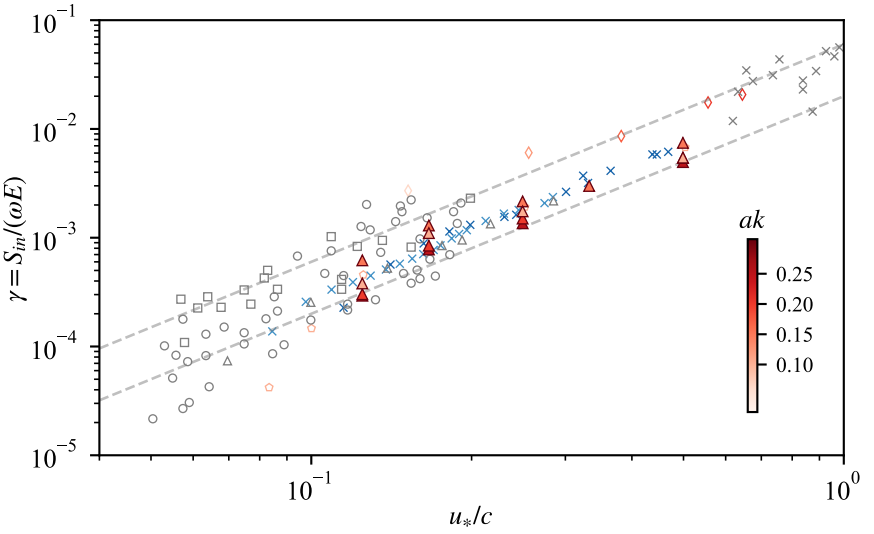

FIGURE 10. Growth rate parameter γ as function of inverse wave age u_*/c. The value of ak is denoted with the color scale whenever they can be identified. Numerical works: blue crosses, Yang *et al.* (2013) with JONSWAP spectrum; open triangles, Kihara *et al.* (2007), $ak = 0.1$. Experimental works: open diamonds, Buckley *et al.* (2020), ak values as the colours indicate; grey symbols: data compiled by Plant (1982) with no steepness information. Dotted lines, the range of β proposed by Plant (1982) based on empirical evidence.

wave age, as already discussed by Peirson & Garcia (2008); Buckley *et al.* (2020). The steepness is indicted in figure 10 with different shades of red for the data sets where the wave steepness can be identified. As we have mentioned, the assumption that the wave drag force scales with the steepness $(ak)^2$ does not hold for moderate to high steepness $(ak > 0.15)$.

The other factor is again, the uncertainty in the pressure-slope correlation (1.1) measurements. The data sets compiled by Plant (1982) were all obtained by measuring the aerodynamic pressure, with either fixed or wave following probes. This is to some extent due to the difficulty in directly measuring the wave growth as an alternative: for the fast moving waves, measuring the extremely small growth in amplitude is prone to errors; and for the less controlled field campaigns, it is hard to single out the wind input from the nonlinear interactions and dissipation. It is of crucial importance, therefore, that we find ways to quantity the uncertainties in these pressure measurements.

In summary, the $(u_*/c)^2$ scaling in figure 10, despite being robust because of the normalisation, inherits the uncertainty reflected in figure 8. The normalisation of S_{in} by ω and E following (1.7) is questionable with the growth rate being very small due to the small density ratio ρ_a/ρ_w so that the exponential growth cannot be verified in a convincing way; and the normalisation makes the γ parameter too skewed by the wave characteristics.

We want to mention that it remains to be studied how the results from the current study and the other lab experiments with nearly monochromatic wave trains can be extended to broadband ocean waves spectrum. The method to date (Snyder *et al.* 1981; Donelan *et al.* 2006; Yang *et al.* 2013) is to keep the linear assumption, and the correlation term 1.1 becomes the cross-spectrum

$$Q(\omega) = \langle p_s(\omega) h_w(\omega) * \rangle. \tag{5.6}$$

Interestingly, the only numerical study of a broad spectrum wave field from Yang *et al.* (2013) (blue crosses) reported growth rate of very similar magnitude to our study. The numerical methods are very different: the points from Yang *et al.* (2013) are from computing (5.6) in one run for different wave frequency ω, while the points in our study are from different runs with different initial c/u_* and ak. The steepness $a(\omega)k$ is not reported in Yang *et al.* (2013), therefore it is hard to draw a definite conclusion.

5.3. *The range of phase shift ϕ_p and implications for potential theories*

Finally, we discuss the implication of numerical results for different theories mentioned in the introduction §1.3. The air pressure distribution is of critical importance to understanding both the wave growth and the wave drag force. It also provides insights into the airflow structure, and therefore can be used to validate or invalidate theories. By comparing our real number representation (4.2), (4.6) to the complex number representation (1.4) there is the correspondence that

$$\beta = P\sin(\phi_{p1}),\ \alpha = P\cos(\phi_{p1}) \tag{5.7}$$

and

$$\phi_{p1}\begin{cases} = \pi/2 & \text{if } \alpha = 0 \\ \in (0,\pi/2) & \text{if } \alpha/\beta > 0 \\ \in (\pi/2,\pi) & \text{if } \alpha/\beta < 0 \end{cases} \tag{5.8}$$

We have based the discussion around the imaginary part of the pressure distribution β, which is the 90° out of phase part with the surface (i.e. in phase with the surface slope). It is always positive for the slow moving waves because of the direction of the energy flux. The real part α, although not contributing to the growth, is informative if we want to determine the phase ϕ_p.

There has not been much discussion on α, although recently Bonfils *et al.* (2021) used an asymptotic method to solve the Rayleigh equation and they pointed out that the real part α, which is often neglected, changes the wave phase speed, and that α can be positive. They have also argued that for strong forcing case, α is around 0, which validates Jeffrey's sheltering hypothesis. This observation agrees with our results. However, the phase shift reported in different experiments are usually in the $(\pi/2,\pi)$ range (Donelan *et al.* 2006; Grare 2009). Since our data are in excellent agreement with Kihara *et al.* (2007) on the phase shift, it suggests that some processes from the laboratory experiments are different than in these numerical simulation (which could be related to three dimensional small scale wave structure).

To summarize, the 90° phase shift, together with the pressure distribution that closely resembles a separated flow supports the Jeffrey's sheltering hypothesis for the strongly forced waves ($c/u_* \leqslant 2$). It is also where we see the smallest S_p/S_{in} ratio, which indicates that the wave coherent viscous stress starts to play a role. The effect of viscous shear stress can be included in the sheltering parameter (1.3) as Jeffrey's original scaling analysis does not exclude the viscous shear stress. The transitional regime ($2 \leqslant c/u_* \leqslant 4$) results in $\phi_{p1} \in (0,\pi/2)$. Only based on the phase shift, it does not seem to be explained by any existing theories, since both Miles's critical layer theory and Belcher's non-separated sheltering theory predict a negative α. Above the intermediate wave regime ($c/u_* \geqslant 8$), the phase shift ϕ_{p1} becomes slightly above 90°, which suggests that the above two theories could potentially apply.

6. Conclusion

We have presented direct numerical simulations of wind waves forced by a turbulent boundary layer, by solving the two-phase Navier-Stokes equations. Leveraging these fully resolved and coupled two-phase DNS, we directly compare the wave energy growth against the pressure input. We discuss the detailed pressure distribution (amplitude and phase) together with the integral quantities (drag force and energy input rate), for a wide range of wave steepness ak and wave age c/u_*. The wave energy input rate is closely linked to the drag force and we discuss the scalings of the drag force and energy input rate with both ak and c/u_*. The pressure distribution at the surface is of particular interest because it gives rise to both the wave growth and the wave drag force, and is a quantity extremely hard to measure experimentally. Our results compare well to previous experimental and numerical works and feed into the ongoing discussions on the exact mechanism responsible for wave growth under various wind forcing regimes. In the strongly forced case, the pressure forcing agrees with the description of the sheltering effect proposed by Jeffrey.

Acknowledgements

This work was supported by the National Science Foundation (Physical Oceanography) under Grant No. 1849762 to L.D. and the Cooperative Institute for Earth System modeling between Princeton and the Geophysical Fluid Dynamics Laboratory (GFDL) NOAA. Computations were partially performed using the Extreme Science and Engineering Discovery Environment (XSEDE), which is supported by NSF Grant No. ACI-1053575; and on resources managed and supported by Princeton Research Computing, a consortium of groups led including the Princeton Institute for Computational Science and Engineering and the Office of Information Technology's High Performance Computing Center and Visualization Laboratory at Princeton University.

We declare no conflict of interest.

Appendix A. Validation of the numerical method

A.1. *Using adaptive mesh refinement in wall turbulence simulation*

In this study, we use Basilisk, a tree-based adaptive mesh refinement (AMR) solver to simulate a turbulent boundary layer flow. AMR exploits the fact that the dynamically active scales in the boundary layer is distributed inhomogeneously, and therefore the computation can be accelerated using a more refined grid near the wall and less refined grid away from the wall. Few work has used AMR to the simulation of a turbulent boundary layer, as far as we know, except for van Hooft *et al.* (2018) where AMR was used to perform large eddy simulation of the atmospheric boundary layer. We note that Perrard *et al.* (2021); Rivière *et al.* (2021); Farsoiya *et al.* (2021) have used AMR for an homogeneous and isotropic turbulence box and demonstrated the accuracy of the methods by considering the second order structure function scaling.

Here, we directly solve the Navier-Stokes equation without any subgrid scale models, and we validate our approach against existing direct numerical simulation from Kim *et al.* (1987) and verify that we reproduce the major features of the canonical turbulent wall-bounded flows.

When simulating wall-bounded turbulent flows, the commonly adopted strategy to increase the near-wall resolution is to use (prescribed) non-uniformly spaced grid in the wall normal direction (e.g. Chebyshev grid in Kim *et al.* (1987)), while keeping the

Case	$(L_x, L_y, L_z)/\delta$	δ_ν/Δ				
Kim *et al.* (1987) ($Re_* = 180$)	$(4\pi, 2\pi, 1)$	$z_1^+ = 20$*				
		N=7	N=8	N=9	N=10	N=11
One-phase ($Re_* = 180$)	$(2, 2, 1)$	0.36	0.71	1.42		
One-phase ($Re_* = 720$)	$(2, 2, 1)$			0.36	0.71	1.42
Two-phase ($Re_* = 720$)	$(2\pi/(2\pi-1), 2\pi/(2\pi-1), 1)$			0.60	1.2	2.4

TABLE 2. The number of grid points per viscous unit (δ_ν/Δ) for different configurations and refinement levels. *The first grid spacing (often denoted as z_1^+) is not exactly comparable to the resolution in the AMR case: because stretched grid used in the spectral method, the grid size increases as it goes away from the wall.

spacing uniform in the streamwise and the spanwise directions. The adaptive mesh of Basilisk uses a different real-time adapting strategy based on the idea of wavelets. It was developed by Popinet (2003, 2009), with recent discussion in Popinet (2015) and van Hooft *et al.* (2018). Briefly speaking, once given the up-sampling (U) and down-sampling (D) operator (which are usually second-order) for computing a certain field (f) when the grid is refined and coarsened, the mesh is controlled by two parameters, the refinement criteria ϵ and the maximum level of refinement N. If the field is of size L_0, the smallest grid size is $\Delta = L_0/2^N$. For a given cell i at level n, the discretization error is given by the absolute difference between the down-sampled and then up-sampled value and the original value (van Hooft *et al.* 2018),

$$\chi_n^i = |U(D(f_n^i)) - f_n^i| \tag{A 1}$$

If χ_n^i is smaller that $2/3\epsilon$, the ith grid is coarsened to level $n-1$; if χ_n^i is bigger that ϵ, the ith grid is coarsened to level $n+1$ (only if $n+1 \ll N$); otherwise the ith grid is kept at level n.

A.2. *Comparison to canonical channel flow with* $Re_* = 180$

To demonstrate that the turbulent boundary layer is resolved properly with the adaptive mesh, we perform a set of single phase channel flow simulations of $Re_* = 180$, and compare our results to the canonical DNS of a channel flow using a spectral method by Kim *et al.* (1987). In addition to validating our numerical method, the cases shown here also provide the benchmarks of how the controlling parameters of the adaptive mesh (i.e. refinement level N and error tolerance ϵ) affect the simulated flow.

The mean horizontal velocity $\bar{u}$ and the rms of velocity fluctuation u_{rms}, v_{rms} and w_{rms} are plotted in figure 11(a) and (b) respectively. They both agree well with Kim *et al.* (1987), although there is a small difference in magnitude in the rms velocity. The mean profile converges at even very coarse grid spacing ($N = 7$), which is an intriguing feature of AMR. The Reynolds stress shown by figure 12 also agrees with the reference case from Kim *et al.* (1987), despite taking longer to converge.

Notice that the refinement criteria ϵ has the same unit as the field f. In the DNS of a turbulent channel flow case, we have found by trial and error that the ϵ value that works the best for the velocity field is around $0.3u_*$. It refines the near wall region without too much refinement in the centre of the channel. This is expected because the friction

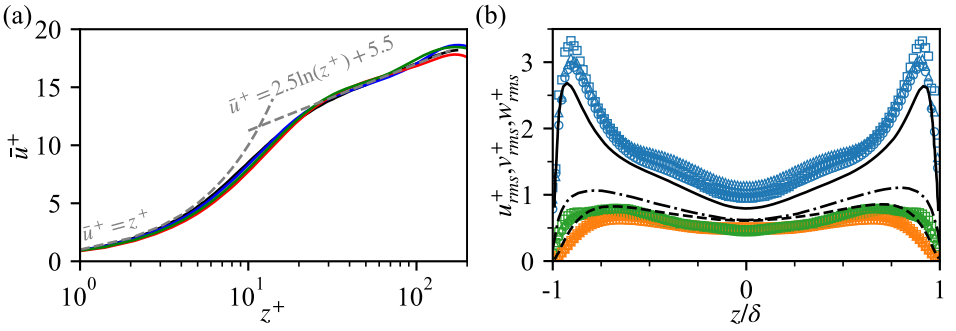

FIGURE 11. Turbulence statistics of one-phase channel flow, $N = 9$ and $\epsilon = 0.3u_*$. (a) Mean horizontal velocity in wall unit. $z^+ = z/\delta_\nu$; $\bar{u}^+ = \bar{u}/u_*$. (b) Velocity fluctuation. Blue: $u^+_{rms} = u_{rms}/u_*$; orange: $v^+_{rms} = v_{rms}/u_*$; green: $w^+_{rms} = w_{rms}/u_*$. Black lines in both (a) and (b) are from Kim *et al.* (1987).

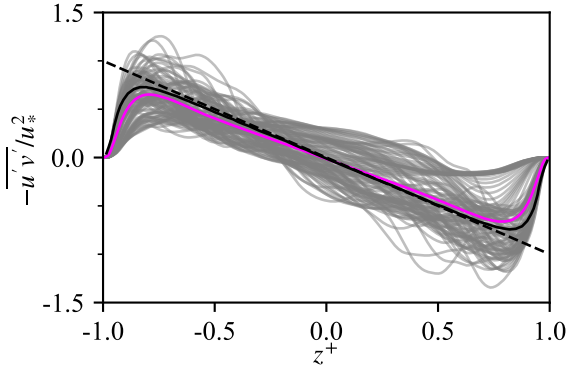

FIGURE 12. The Reynolds stress $-\overline{u'v'}$ normalised by total wall stress. The solid black line is from Kim *et al.* (1987). The computational domain in the AMR solver is by default cubed, and therefore limited in the streamwise and spanwise sizes. It causes the second order statistics to converge more slowly. Averaged over 10 eddy turnover time T_e, with T_e defined as $T_e = \delta/u_*$.

velocity u_* is the characteristic velocity scale in the boundary, but we comment that the particular prefactor is likely to change for different configurations and Reynolds numbers.

A.3. *Convergence between one-phase and two-phase cases at $Re_* = 720$*

The cases in the paper are run with the two-phase configuration at $N = 10$ and $\epsilon = 0.3u_*$ (see table 2). We have also tested that the one-phase and two-phase flat wall cases agree with each other, and that the mean profile converges at $N = 9, 10, 11$ (see figure 13 (a)). Figure 13 (b) shows how the rms velocity is effected by the maximum refinement level N and error tolerance ϵ. A slightly larger ϵ results in higher horizontal rms velocity in the outer region. Overall the difference is small and the rms velocity is well converged between different N and ϵ.

A.4. *Convergence verification for the moving wave cases*

We verify that the wave averaged quantities (energy and wave drag force) exhibit good convergence between the $N = 10$ and 11 cases, as we show in figure 14. The results are also not sensitive when the Bond number is increased, as shown with different shades of green, confirming that the results in the paper apply in the gravity-capillary to gravity

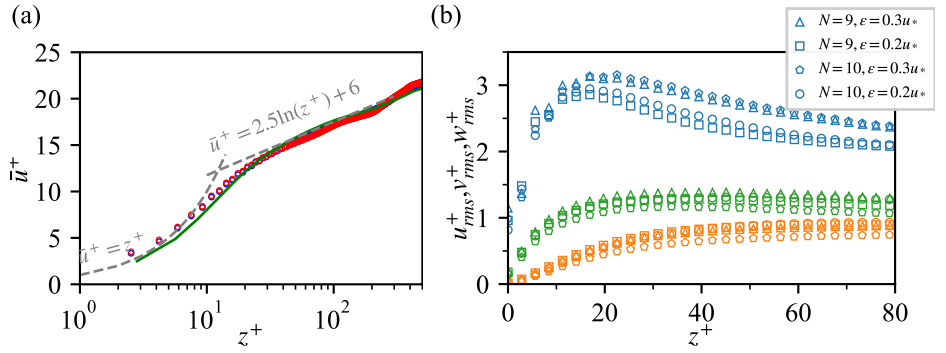

FIGURE 13. (a) Mean horizontal velocity for the $Re_* = 720$ cases. Green curve: single phase with $N = 9$, $\epsilon = 0.3u_*$; red and blue dots: two phase cases with flat surface (the same configuration as all the moving wave cases), $\epsilon = 0.1u_*$ at $N = 10$ and 11 respectively. (b) The rms velocity for the single phase cases, under different maximum refinement levels N and error tolerances ϵ.

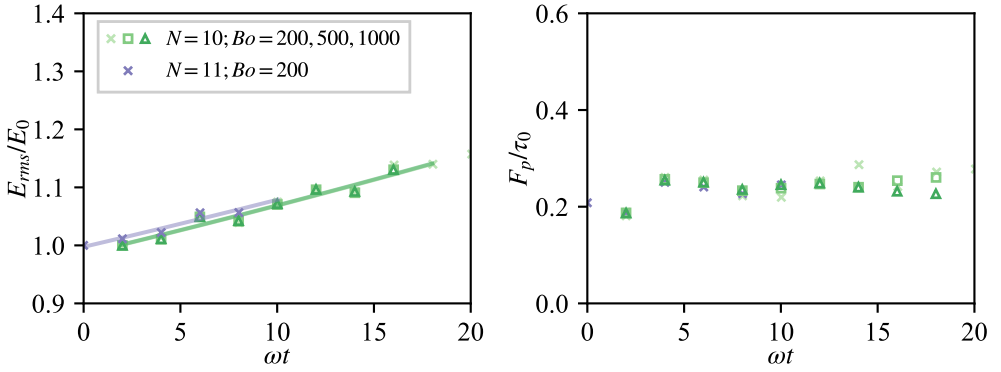

FIGURE 14. Left: convergence of the wave energy for different refinement levels N and Bond numbers Bo. The energy evolution converges at higher Bond number. Right: convergence of the wave drag force. The symbols are the same with the left plot. $ak = 0.15$, $c/u_* = 2$.

wave regime. Some variations in the wave drag force are seen, related to the chaotic variations of the instantaneous flow.

REFERENCES

AIYER, A. K., DEIKE, L. & MUELLER, M. E. 2021 A sea surface-based drag model for Large Eddy Simulation of wind-wave interaction. *arXiv:2112.06783 [physics]* , arXiv: 2112.06783.

BELCHER, S.E. 1999 Wave growth by non-separated sheltering. *Eur. J. Mech. B Fluids* **18** (3), 447–462.

BELCHER, S. E. & HUNT, J. C. R. 1993 Turbulent shear flow over slowly moving waves. *J. Fluid Mech.* **251**, 109–148.

BONFILS, A. F., MITRA, D., MOON, W. & WETTLAUFER, J. S. 2021 Asymptotic interpretation of the Miles mechanism of wind-wave instability. *arXiv:2107.06844 [physics]* , arXiv: 2107.06844.

BUCKLEY, M. P., VERON, F. & YOUSEFI, K. 2020 Surface viscous stress over wind-driven waves with intermittent airflow separation. *J. Fluid Mech.* p. 28.

Cavaleri, L., Fox-Kemper, B. & Hemer, M. 2012 Wind Waves in the Coupled Climate System. *Bull. Amer. Meteor. Soc.* **93** (11), 1651–1661.

Deike, L. 2022 Mass Transfer at the Ocean–Atmosphere Interface: The Role of Wave Breaking, Droplets, and Bubbles. *Annu. Rev. Fluid Mech.* **54** (1), 191–224.

Deike, L., Melville, W. K. & Popinet, S. 2016 Air entrainment and bubble statistics in breaking waves. *J. Fluid Mech.* **801**, 91–129.

Deike, L., Popinet, S. & Melville, W. K. 2015 Capillary effects on wave breaking. *J. Fluid Mech.* **769**, 541–569.

Deskos, G., Lee, J. C. Y., Draxl, C. & Sprague, M. A. 2021 Review of wind-wave coupling models for large-eddy simulation of the marine atmospheric boundary layer. *Journal of the Atmospheric Sciences* .

Donelan, M. A., Babanin, A. V., Young, I. R. & Banner, M. L. 2006 Wave-Follower Field Measurements of the Wind-Input Spectral Function. Part II: Parameterization of the Wind Input. *J. Phys. Oceanogr.* **36** (8), 1672–1689.

Farsoiya, P. K., Popinet, S. & Deike, L. 2021 Bubble-mediated transfer of dilute gas in turbulence. *J. Fluid Mech.* **920**, A34.

Fedorov, A. V. & Melville, W. K. 1998 Nonlinear gravity–capillary waves with forcing and dissipation. *J. Fluid Mech.* **354**, 1–42.

Funke, C. S., Buckley, M. P., Schultze, L. K. P., Veron, F., Timmermans, M.-L. E. & Carpenter, J. R. 2021 Pressure fields in the airflow over wind-generated surface waves. *J. Phys. Oceanogr.* .

Fuster, D. & Popinet, S. 2018 An all-Mach method for the simulation of bubble dynamics problems in the presence of surface tension. *Journal of Computational Physics* **374**, 752–768.

Grare, L. 2009 étude des interactions océan-atmosphère à proximité immédiate de l'interface: Application aux vagues de vent et aux vagues extrêmes. PhD thesis, Université de la Méditerranée-Aix-Marseille II.

Grare, L., Peirson, W. L., Branger, H., Walker, J. W., Giovanangeli, J.-P. & Makin, V. 2013 Growth and dissipation of wind-forced, deep-water waves. *J. Fluid Mech.* **722**, 5–50.

Janssen, P. 2004 *The Interaction of Ocean Waves and Wind*, 1st edn. Cambridge University Press.

Jeffreys, H. 1925 On the Formation of Water Waves by Wind. *Proceedings of the Royal Society A: Mathematical, Physical and Engineering Sciences* **107** (742), 189–206.

Kawai, S. 1979 Generation of initial wavelets by instability of a coupled shear flow and their evolution to wind waves. *J. Fluid Mech.* **93** (04), 661.

Kihara, N., Hanazaki, H., Mizuya, T. & Ueda, H. 2007 Relationship between airflow at the critical height and momentum transfer to the traveling waves. *Phys. Fluids* **19** (1), 015102.

Kim, J., Moin, P. & Moser, R. 1987 Turbulence statistics in fully developed channel flow at low Reynolds number. *J. Fluid Mech.* **177**, 133–166.

Lamb, H. 1993 *Hydrodynamics*. Cambridge university press.

Li, T. & Shen, L. 2022 The principal stage in wind-wave generation. *J. Fluid Mech.* **934**, A41.

Lin, M.-Y., Moeng, C.-H., Tsai, W.-T., Sullivan, P. P. & Belcher, S. E. 2008 Direct numerical simulation of wind-wave generation processes. *J. Fluid Mech.* **616**, 1–30.

Mastenbroek, C., Makin, V. K., Garat, M. H. & Giovanangeli, J. P. 1996 Experimental evidence of the rapid distortion of turbulence in the air flow over water waves. *J. Fluid Mech.* **318** (-1), 273.

Melville, W. K. & Fedorov, A. V. 2015 The equilibrium dynamics and statistics of gravity–capillary waves. *J. Fluid Mech.* **767**, 449–466.

Miles, J. W. 1957 On the generation of surface waves by shear flows. *J. Fluid Mech.* **3** (02), 185.

Mostert, W. & Deike, L. 2020 Inertial energy dissipation in shallow-water breaking waves. *J. Fluid Mech.* **890**, A12.

Mostert, W., Popinet, S. & Deike, L. 2022 High-resolution direct simulation of deep water breaking waves: Transition to turbulence, bubbles and droplet production. *arXiv:2103.05851 [physics]* , arXiv: 2103.05851.

Peirson, W. L. & Garcia, A. W. 2008 On the wind-induced growth of slow water waves of finite steepness. *J. Fluid Mech.* **608**, 243–274.

Perrard, S., Rivière, A., Mostert, W. & Deike, L. 2021 Bubble deformation by a turbulent flow. *J. Fluid Mech.* **920**, A15.

Piomelli, U. & Balaras, E. 2002 Wall-Layer Models for Large-Eddy Simulations. *Annu. Rev. Fluid Mech.* **34** (1), 349–374.

Plant, W. J. 1982 A relationship between wind stress and wave slope. *J. Geophys. Res.* **87** (C3), 1961.

Popinet, S. 2003 Gerris: A tree-based adaptive solver for the incompressible Euler equations in complex geometries. *Journal of Computational Physics* **190** (2), 572–600.

Popinet, S. 2009 An accurate adaptive solver for surface-tension-driven interfacial flows. *J. Comput. Phys* **228** (16), 5838–5866.

Popinet, S. 2015 A quadtree-adaptive multigrid solver for the Serre–Green–Naghdi equations. *Journal of Computational Physics* **302**, 336–358.

Popinet, S. 2018 Numerical Models of Surface Tension. *Annu. Rev. Fluid Mech.* **50** (1), 49–75.

Rivière, Aliénor, Mostert, Wouter, Perrard, Stéphane & Deike, Luc 2021 Sub-Hinze scale bubble production in turbulent bubble break-up. *J. Fluid Mech.* **917**, A40.

Shemer, L. 2019 On Evolution of Young Wind Waves in Time and Space. *Atmosphere* **10** (9), 562.

Snyder, R. L., Dobson, F. W., Elliott, J. A. & Long, R. B. 1981 Array measurements of atmospheric pressure fluctuations above surface gravity waves. *J. Fluid Mech.* **102**, 1–59.

Sullivan, P. P. & McWilliams, J. C. 2010 Dynamics of Winds and Currents Coupled to Surface Waves. *Annu. Rev. Fluid Mech.* **42** (1), 19–42.

Tsai, W.-T., Chen, S.-M., Lu, G.-H. & Garbe, C. S. 2013 Characteristics of interfacial signatures on a wind-driven gravity-capillary wave: CHARACTERISTIC SIGNATURES ON A WIND WAVE. *J. Geophys. Res. Oceans* **118** (4), 1715–1735.

van Hooft, J. A., Popinet, S., van Heerwaarden, C. C., van der Linden, S. J. A., de Roode, S. R. & van de Wiel, B. J. H. 2018 Towards Adaptive Grids for Atmospheric Boundary-Layer Simulations. *Boundary-Layer Meteorol* **167** (3), 421–443.

Wu, J. 1968 Laboratory studies of wind–wave interactions. *J. Fluid Mech.* **34** (1), 91–111.

Wu, J. & Deike, L. 2021 Wind wave growth in the viscous regime. *Phys. Rev. Fluids* **6** (9), 094801.

Yang, D., Meneveau, C. & Shen, L. 2013 Dynamic modelling of sea-surface roughness for large-eddy simulation of wind over ocean wavefield. *J. Fluid Mech.* **726**, 62–99.

Yang, D. & Shen, L. 2010 Direct-simulation-based study of turbulent flow over various waving boundaries. *J. Fluid Mech.* **650**, 131–180.

Zdyrski, T. & Feddersen, F. 2020 Wind-induced changes to surface gravity wave shape in deep to intermediate water. *J. Fluid Mech.* **903**, A31.

Zhang, B., Popinet, S. & Ling, Y. 2020 Modeling and detailed numerical simulation of the primary breakup of a gasoline surrogate jet under non-evaporative operating conditions. *International Journal of Multiphase Flow* **130**, 103362.